A Model for the Three-Dimensional Structure of Human Plasma Vitronectin from Small-Angle Scattering Measurements†

Gary W. Lynn,‡ William T. Heller,‡ Anand Mayasundari,§ Kenneth H. Minor,§ and Cynthia B. Peterson*,§

Department of Biochemistry and Cellular and Molecular Biology and Center of Excellence in Structural Biology, University of Tennessee, Knoxville, Tennessee 37996, and Center for Structural Molecular Biology and Condensed Matter Sciences Division, Oak Ridge National Laboratory, Oak Ridge, Tennessee 37831

Received August 2, 2004; Revised Manuscript Received September 15, 2004

ABSTRACT: Small-angle X-ray scattering (SAXS) measurements were used to characterize vitronectin, a circulatory protein found in human plasma that functions in regulating cell adhesion and migration, as well as proteolytic cascades that affect blood coagulation, fibrinolysis, and pericellular proteolysis. SAXS measurements were taken over a 3-fold range of protein concentrations, yielding data that characterize a monodisperse system of particles with an average radius of gyration of 30.3 ± 0.6 Å and a maximum linear dimension of 110 Å. Shape restoration was applied to the data to produce two models of the solution structure of the ligand-free protein. A low-resolution model of the protein was generated that indicates the protein to be roughly peanut-shaped. A better understanding of the domain structure of vitronectin resulted from low-resolution models developed from available high-resolution structures of the domains. These domains include the N-terminal domain that was determined experimentally by NMR [Mayasundari, A., Whittemore, N. A., Serpersu, E. H., and Peterson, C. B. (2004) *J. Biol. Chem. 279*, 29359−29366] and the docked structure of the central and C-terminal domains that were determined by computational threading [Xu, D., Baburaj, K., Peterson, C. B., and Xu, Y. (2001) *Proteins: Struct., Funct., Genet. 44*, 312−320]. This model provides an indication of the disposition of the central domain and C-terminal heparin-binding domains of vitronectin with respect to the N-terminal somatomedin B (SMB) domain. This model constructed from the available domain structures, which agrees with the low-resolution model produced from the SAXS data, shows the SMB domain well separated from the central and heparin-binding domains by a disordered linker (residues 54−130). Also, binding sites within the SMB domain are predicted to be well exposed to the surrounding solvent for ease of access to its various ligands.

Vitronectin is a glycoprotein from human plasma that controls several physiological processes, including blood coagulation, fibrinolysis, cell adhesion and migration, tumor metastasis, and tissue remodeling, in conjunction with its various ligands (*1*−*4*). These ligands, which are structurally dissimilar, include heparin, plasminogen activator inhibitor type 1 (PAI-1),[1] the antithrombin−thrombin complex, integrins, the urokinase receptor (uPAR), and collagen. Additionally, vitronectin, which was originally identified as "S-protein" (for the "soluble" protein of complement), is involved in the modulation of the cellular immune response (*5*).

Vitronectin has been extensively studied, with much of the work focusing on identifying binding sites for the various ligands (for reviews, see refs *1* and *6*). A rough sense of the organization of vitronectin has resulted from a combination of experimental techniques, including immunochemical studies, sequence comparisons, limited proteolysis, peptide mapping, and investigations using recombinant fragments. Given the wide array of binding partners, the protein appears to be organized into distinct domains with associated functional properties. The first 44 amino acids of the 51-residue N-terminal domain are identical to those of somatomedin B (SMB), a circulating protein of unknown function that is somewhat homologous to growth factor-like domains (*7*). This N-terminal domain contains binding sites for PAI-1 (*8*−*11*), the integrins (*10*, *12*), and uPAR (*13*). Residues 54−130 comprise a linker region, which is proposed to be unstructured (*14*). The central domain is composed of residues 131−323 and is thought to provide binding sites for bacteria (*15*−*17*). The C-terminal domain, including residues 354−456, houses the heparin binding site on vitronectin (*11*, *18*, *19*) and also contains potential binding sites for plasminogen (*20*), complement factors (*21*), and perforin (*21*, *22*). There is also a possible secondary weak binding site for PAI-1 (*23*−*25*) within the C-terminal domain. The distribution of these four domains along the linear chain of vitronectin is shown in Figure 1A.

† This research was supported by National Institutes of Health Grant HL50676 (C.B.P.) and by the Office of Biological and Environmental Research of the U. S. Department of Energy, under Contract DE-AC05-00OR22725 with Oak Ridge National Laboratory, managed and operated by UT-Batelle, LLC. A.M. was supported by a Postdoctoral Fellowship 0120344B from the American Heart Association, Southeast Regional Affiliate.

* To whom correspondence should be addressed. E-mail: cynthia_peterson@utk.edu. Phone: (865) 974-5148. Fax: (865) 974-6306.

‡ Oak Ridge National Laboratory.

§ University of Tennessee.

[1] Abbreviations: PAI-1, plasminogen activator inhibitor type 1; SMB, somatomedin B; uPAR, urokinase-type plasminogen activator receptor; NMR, nuclear magnetic resonance; SAXS, small-angle X-ray scattering; ECM, extracellular matrix.

10.1021/bi048347s CCC: $30.25
Published on Web 12/17/2004

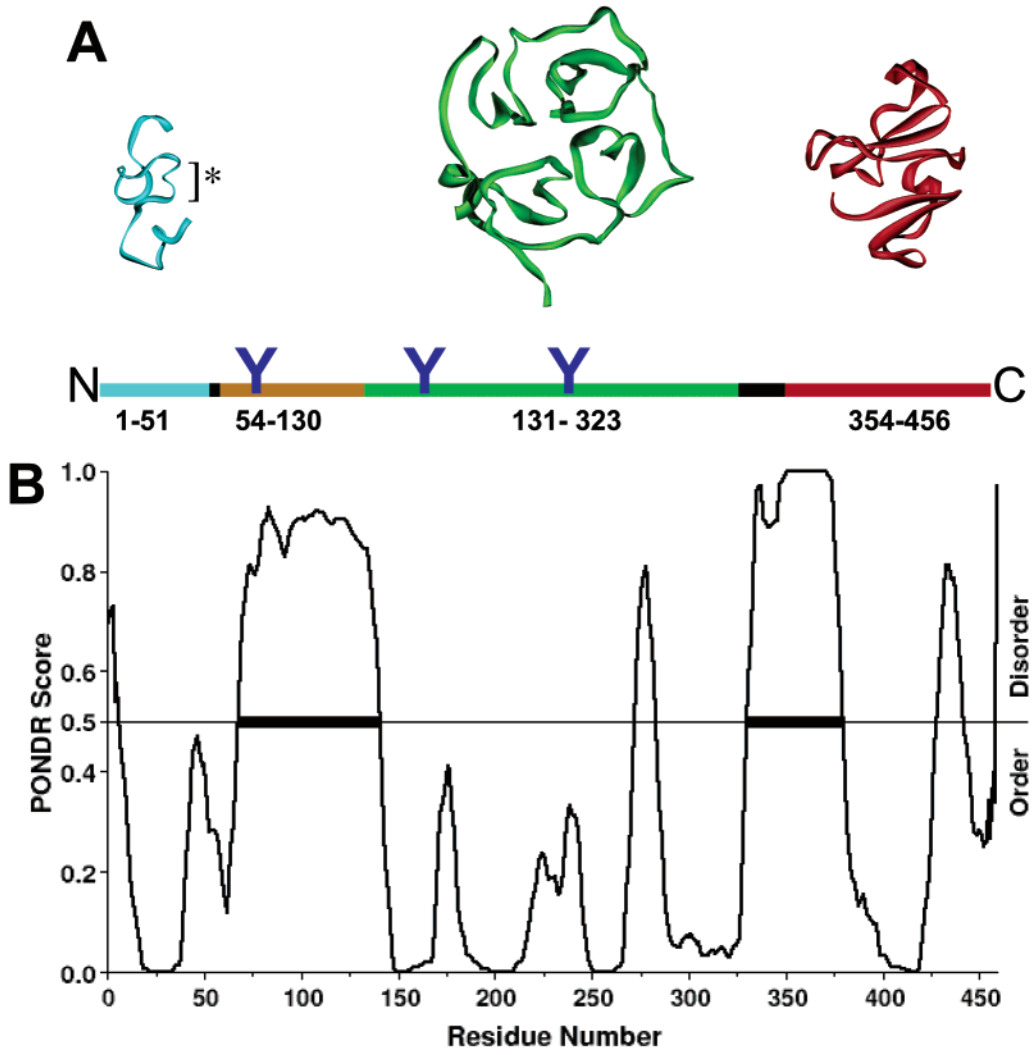

FIGURE 1: Domain structure of vitronectin. Panel A shows the linear sequence of vitronectin spanning 459 amino acids from the N- to C-terminus with domains highlighted and numbered below the line: N-terminal SMB domain (cyan), connecting region (amber), central domain (green), and C-terminal domain (red). Sites of carbohydrate attachment are shown as the blue "Y" structures. Two short segments that lie at the junction of the domains are shown as solid black lines. High-resolution structures for three of these domains are shown above the linear sequence, using the same color scheme. The structure for the N-terminal SMB domain was determined recently using NMR (*10*), with an asterisk denoting the single α-helix in this small domain. Structures for the central and C-terminal domains are predicted structures from threading (*14*). Panel B shows the prediction of disordered regions within the vitronectin polypeptide using PONDR. The PONDR score is plotted relative to each residue position number within the full-length vitronectin sequence of 459 amino acids. The disorder threshold is indicated by the horizontal line at a score of 0.5. Predicted regions of disorder are denoted with solid black bars spanning regions of >20 consecutive amino acids with a PONDR score above the threshold.

Determining the three-dimensional arrangement of this multidomain protein is of keen interest to researchers because of the need to characterize ligand binding, conformational changes, and self-association of vitronectin. The protein has not been successfully crystallized, and the structure of the intact protein, containing 459 residues, is too large for high-resolution structural determination by NMR. Previously, we used computational methods to derive a model for the vitronectin domains using threading and docking algorithms (*14*). This work predicted a *β*-propeller-type structure for the central domain and an incomplete propeller, comprising only half of the propeller structure equivalent to two *β*-"blades," for the C-terminal domain. The threaded structures for these two domains are shown above the corresponding regions of linear sequence in Figure 1A. The docked structure of the central and C-terminal domains predicted a heparin-binding surface that was compatible with a variety of experimental criteria (*14*). However, the computational approach was less satisfactory in predicting the fold of the N-terminal SMB domain. Recently, we determined the disulfide-bonding pattern (*7*) and determined the structure of the SMB domain isolated from human plasma vitronectin by NMR (*10*). Shown in Figure 1A is this structure for the SMB domain, which consists mainly of random coils, but contains a sole α-helix that constitutes an important feature in the binding of PAI-1 and uPAR. This single-turn helix is also present in the X-ray structure of a recombinant SMB determined in a cocrystal with PAI-1 (*26*). In contrast, the remainder of the structure, including the disulfide pairings, differs comparing the SMB domain from plasma vitronectin to either of the two recombinant counterparts (*26*−*28*). While this structural work is important with regard to the behavior of the independent domains, it falls short for understanding the domain organization and function of the full-length protein.

In this study, we present our results from small-angle X-ray scattering (SAXS) experiments on the intact vitronectin monomer isolated from human plasma. In addition to traditional analysis methods, two approaches to developing structural models from the data were taken. The first approach employed the program GA_STRUCT (*29*) which produced *ab initio* models from the measured SAXS data. The result is a low-resolution model that describes the boundary of the space occupied by the protein. As a second approach to modeling the SAXS data, CONTRAST (*30*) was used to develop a low-resolution model assembled from the high-resolution structures of the domains determined by NMR and predicted by threading (Figure 1A). The resulting models predict the N-terminal domain to be spatially separated from the central and heparin-binding domains by the linker sequence. The models are useful for understanding the relative disposition of sites for various binding partners of vitronectin, including PAI-1, uPAR, integrins, and heparin. The SAXS experiments and modeling provide insight into the structural organization of vitronectin, which has been poorly understood since a high-resolution three-dimensional structure has yet to be determined.

MATERIALS AND METHODS

Protein Purification. Human plasma vitronectin was isolated by a modification of the procedure of Dahlback and Podack (*31*), as described by Zhuang et al. (*32*). Purified vitronectin was stored as a suspension in saturated ammonium sulfate at 4 °C until it was used.

Small-Angle X-ray Scattering Measurements. Small-angle X-ray scattering (SAXS) measurements were carried out using the Oak Ridge National Laboratory (ORNL) 10 m SAXS camera (*33*). A rotating anode that produces Cu $K_{\alpha 1}$ radiation ($\lambda = 1.54$ Å) generates the incident beam with a source power of 2.8 kW (40 kV, 70 mA). A sample-to-detector distance of 3.12 m was used to give a q-range from 0.0068 to 0.16 Å^{-1}. The vitronectin samples were prepared in 300 μL of a phosphate-buffered saline solution (PBS) containing 10 mM dibasic sodium phosphate and 2 mM monobasic potassium phosphate and 0.14 M NaCl at pH 7.4 to give final concentrations of 2.2 and 3.3 mg/mL. These solutions were then transferred to a flattened, 1 mm thick glass capillary for measurement that has an X-ray transmission of 0.70 when empty and provides a scattering volume of approximately 3.1 mm^3. During the measurements, the sample was kept at a constant temperature of 17 ± 1.0 °C. Two-dimensional scattering intensity data were collected and corrected for empty glass capillary and buffer solution scattering, background counts, and detector uniformity. Vitreous carbon was measured as a secondary standard to convert the measured intensities to an absolute differential scattering cross section per unit volume of sample (*34*). The two-dimensional data were circularly averaged to produce one-dimensional scattering intensity profiles. SAXS data were also collected on the X21 beam line at the National Synchrotron Light Source (Brookhaven National Laboratory, Upton, NY) on vitronectin samples with concentrations of 3.5, 2.0, and 1.0 mg/mL in PBS with NaCl ranging from 0.14 to 0.28 M. These data were reduced by a similar procedure.

Small-Angle X-ray Scattering Data Analysis. Small-angle scattering of X-rays arises from fluctuations that produce differences in electron density, such as particles in solution. The angular distribution of the scattered intensity reflects the structure of the particle over length scales typically ranging from 5 to 1000 Å. The scattered intensity is measured as a function of the scattering vector, q. If 2θ is the scattering angle from the incident beam direction, then

$$q = \frac{4\pi \sin(\theta)}{\lambda} \tag{1}$$

where λ is the incident wavelength. The scattering intensity $I(q)$ from a particle in solution is maximal when $q = 0$ and decays with a rate that depends on the size and shape of the particle. If one considers a particle in solution to be a two-phase system, i.e., particle and solvent, then the scattering length density of the solvent must also be taken into account according to eq 2 (*35*, *36*)

$$I(q) = n\langle|\int_V[\rho(r) - \rho_s]e^{-iqr}\, d^3r|^2\rangle \tag{2}$$

where $I(q)$ is the scattered intensity, n is the number of particles per unit volume, $\rho(r)$ is the scattering length density of the particle, ρ_s is the scattering length density of the solvent, and r denotes the relative position within the scattering particle. The integral is over the volume of the particle. The integral is averaged over time, all orientations, and the ensemble of structures present in the solution.

For a dilute, monodisperse solution of homogeneous particles, the intensity $I(q)$ is related to the radius of gyration (R_g) of a single particle by the Guinier law (*35*):

$$\ln[I(q)] = \ln[I(0)] - \frac{(qR_g)^2}{3} \tag{3}$$

Guinier fitting is confined to cases where $qR_g < 1.3$. Guinier fitting also provides evidence of the presence or absence of aggregation, which manifests as an upturn in the low-q data, or artifacts due to interparticle interference, which manifest as a downturn in the low-q data.

The forward scatter, $I(0)$, can be used to determine the molecular mass of the scattering particle when the measured intensity is converted to absolute units. It is known that $I(0) \propto cM_W$ (*35*), where c is the concentration and M_W is the molecular mass of the scattering particle. Determining the molecular mass of the scattering particle from $I(0)$ provides a secondary check on the monodispersity of the sample.

Additional analysis can be performed to provide more information about the shape of the scattering particle. It is convenient to invert eq 2, thereby generating the distance distribution function $P(r)$ from the experimental $I(q)$ curve using the Fourier transform in eq 4.

$$P(r) = \frac{1}{2\pi^2}\int_0^\infty dq\,(qr)I(q)\sin(qr) \tag{4}$$

The Moore algorithm (*37*) was used to determine $P(r)$ from the scattering intensity $I(q)$. $P(r)$ is the distribution of interparticle vector lengths within a single scattering particle. From $P(r)$, it is possible to determine d_{max}, the maximum linear dimension of the particle.

Structural Modeling. *Ab initio* models of vitronectin were generated from the SAXS profile using GA_STRUCT (*29*), which produces a set of independent models composed of overlapping spheres that fit the measured SAXS intensity.

The quality of the fit of each individual model intensity profile, calculated from the $P(r)$ of the model and the inverse of the Fourier transform defined in eq 4, is evaluated using the parameter F defined in eq 5.

$$F = \frac{1}{N_{pts}}\left\{\sum_{N_{pts}} \frac{[I(q) - I_m(q)]^2}{\sigma(q)^2}\right\} \quad (5)$$

where N_{pts} is the number of points in the data set, $I(q)$ and $I_m(q)$ are the experimental and model intensities, respectively, and $\sigma(q)$ is the experimental uncertainty of $I(q)$. The set of models produced by GA_STRUCT is characterized for similarity by overlaying the models onto one another. The parts of the structure that are consistent across the majority of the models, called the consensus envelope, are also an output of the program.

Models were also developed with CONTRAST (*30*), which uses shapes or known structures to model either SAXS or small-angle neutron scattering contrast variation series data. The program determines the optimal fit to the scattering data by minimizing F (eq 5). To model the vitronectin structure, a modified version of CONTRAST was employed that allowed for the connection of carbohydrates. High-resolution structural models exist for the domains of vitronectin (Figure 1A). The NMR structure of N-terminal residues 1−51 (*10*), the SMB domain, was one structure employed in the modeling. The threaded and docked model of the central domain and C-terminal heparin-binding domain (*14*) were also used as an input structure for CONTRAST. To simulate the linker region of vitronectin, which connects the N-terminal and central domains, cylinders were employed in an approach similar to that used previously for protein kinase A (*38*, *39*). The linker cylinder was filled with random points such that the density of points and the volume of cylinders were consistent with the number of atoms contained in the residues missing from the high-resolution structures. Cylinders with radii of 10, 12, 14, 16, 18, and 20 Å were tested. The ends of the cylinders were linked to the appropriate end residues of the SMB domain structure and the central/C-terminal docked structure.

The vitronectin used in this study has three branched chain carbohydrates attached at Asn67, Asn150, and Asn223 (positions for attachment shown in Figure 1A). Structures of the bi- and triantennary carbohydrates were generated using W3-SWEET (*40*), and were connected to the structure at the proper points. Asn67 lies within the missing linker region, so the carbohydrate was connected to the surface of the cylinder at a position along its length in proportion to the position of Asn67 in the linker sequence. $I(q)$ for the models was calculated from the model $P(r)$ functions using the inverse of the Fourier transform defined in eq 4.

Bioinformatic Analyses. PONDR (*41*, *42*) was used to analyze the entire length of the vitronectin polypeptide for predicted regions of disorder. PSIPRED (*43*, *44*) was used to expand the prediction of secondary structure within the linker region of vitronectin (residues 54−130). PSIPRED was run twice. In one run, regions in which the level of sequence complexity was low, i.e., immediately adjacent repeat sequences, were masked out. Such regions were not masked out in the second run of PSIPRED. Ordered structures within proteins form as a result of the specificity imparted by unique sequences of amino acids. Less complex regions lack specificity and hence are often in a disordered state. To check further for structurally disordered regions in the vitronectin linker, GLOBPLOT (*45*) and DISEMBL (*46*) were used with the default options.

RESULTS

Small-Angle X-ray Scattering. SAXS data of vitronectin in a buffer solution (3.3 mg/mL) are plotted in Figure 2A. Figure 2B contains a Guinier plot {ln[$I(q)$] vs q^2} of the SAXS data. The radius of gyration (R_g) is determined to be 30.3 ± 0.6 Å from a straight line fit ($R^2 = 0.924$) in the q^2 range from 0.000300 to 0.00178 Å^{-2}. One important result from this plot is that the vitronectin is well behaved at a concentration of 3.3 mg/mL; i.e., the sample is not aggregated. If the sample were aggregated, the Guinier plot would show that as $q^2 \rightarrow 0$, the scattering intensity would not follow a straight line, but would instead deviate upward. As one can see from Figure 2B, this is clearly not the case. The Guinier plot also does not deviate downward from a straight line as $q^2 \rightarrow 0$, indicating that the data are free from artifacts due to interparticle interference effects. A concentration of 3.3 mg/mL and an $I(0)$ of 0.135, determined from the Guinier fitting, correspond to a molar mass of ∼60 000 g/mol, in agreement with the known molecular weight for vitronectin of 62 000 from analytical ultracentrifugation.[2]

To further validate this result, we measured four additional concentrations of vitronectin on two different instruments. Analyses of the measured SAXS data for the vitronectin samples at concentrations of 3.5, 2.2, 2.0, and 1.0 mg/mL yield the same R_g as the sample at 3.3 mg/mL (within 0.9 Å). Since the R_g is independent of concentration, we can conclude that the vitronectin samples are monodisperse within this concentration range.

The distance distribution function $P(r)$ of vitronectin is shown in Figure 2C. The d_{max} of vitronectin was found to be 110 Å by testing various values until a $P(r)$ was found in which the curve decays smoothly to zero at the maximum dimension. The peak of $P(r)$, which corresponds to the most common vector length within the particle, is at ∼32 Å. The shape of $P(r)$ suggests that vitronectin has a somewhat elongated shape, instead of being a compact, globular particle.

Bioinformatic Analyses. In our previous computational prediction of the domain structure of vitronectin from threading, an extensive linker region between the SMB domain and central domain was not modeled and was thought to be unstructured (*14*). PONDR (*41*, *42*) was initially used to evaluate the entire length of 459 amino acids in vitronectin to gauge regions of predicted disorder. As shown in Figure 1B, there are two regions that are predicted by this algorithm to be flexible and relatively unstructured in vitronectin, one encompassing residues ∼70−130 and a second in the C-terminal region including residues ∼330−370. The first

[2] The molecular weight reported for vitronectin from our initial analyses using sedimentation equilibrium (*49*) was 72 000, using a partial specific volume that is typical for proteins of 0.73 mL/g (*62*). A newer calculation of the partial specific volume that includes the contribution from carbohydrate side chains using SEDNTERP (J. Philo, Alliance Protein Laboratories, Thousand Oaks, CA) indicated a lower value of 0.705 mL/g. The corrected molecular weight using this revised partial specific volume is 62 000.

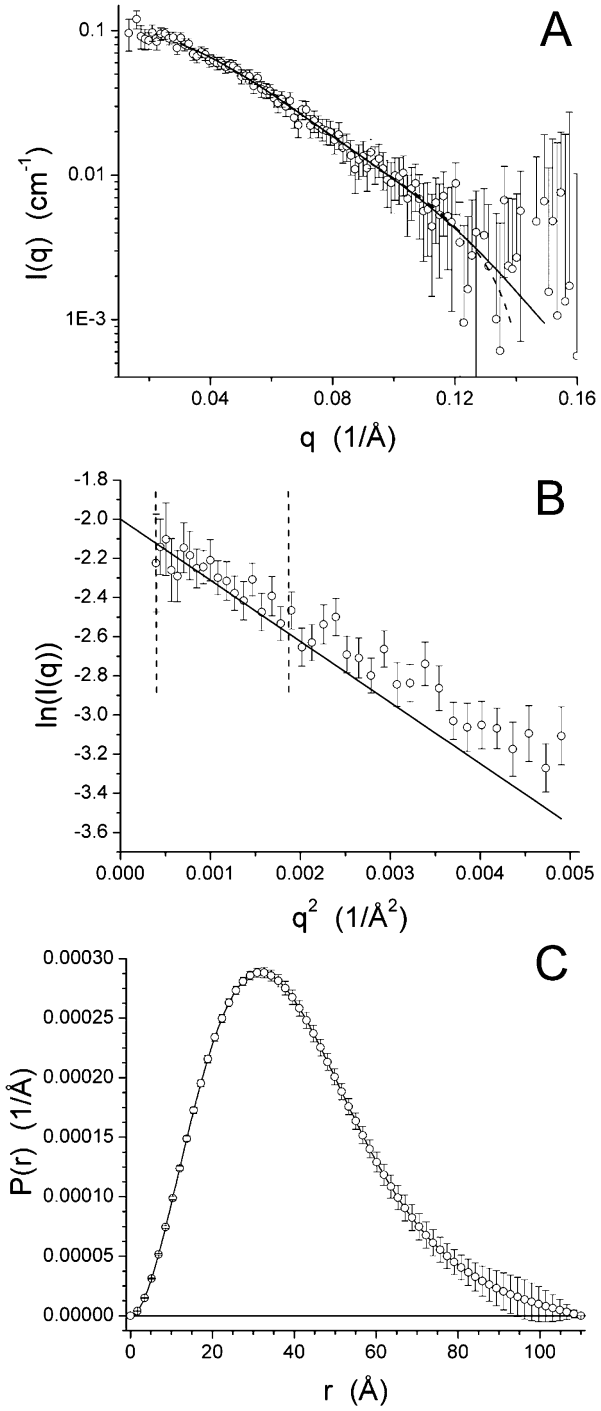

FIGURE 2: (A) Small-angle X-ray scattering intensity data for vitronectin. Vitronectin (3.3 mg/mL) was dialyzed into phosphate-buffered saline (pH 7.4). The circles denote the SAXS data, and the error bars indicate the standard uncertainty in the measurement. The smooth curved line is a sample model intensity profile from the GA_STRUCT (*29*) modeling. The dashed line corresponds to the best-fit model produced by CONTRAST (*30*). (B) Guinier plot of the SAXS intensity data for vitronectin. Data are from panel A. The Guinier fit ($R^2 = 0.924$) gives an R_g of 30.3 ± 0.6 Å. (C) Interparticle vector length distribution, $P(r)$, calculated from SAXS intensity data, $I(q)$, on vitronectin. The data points fit to a smooth curve correspond to a maximum dimension (d_{max}) of 110 Å, and the error bars indicate the standard uncertainty in the measurement.

and most extensive of these loci spans the linker region between the N-terminal SMB domain and the central domain, the sole sequence within vitronectin for which there are no structural models, from either NMR or threading. For a more thorough analysis, PSIPRED (*43*, *44*) was applied to the sequence of the entire linker region (residues 54−130) both with and without the filter to mask low-complexity regions of the sequence. The results were identical with and without the filter turned on, indicating that the sequence contains no low-complexity regions. The entire linker sequence was predicted to be random coils, with the exception of a short helical segment of residues 81−85. Even though the sequence was predominantly coils, the prediction does not necessarily mean that there is a lack of tertiary structure.

GLOBPLOT (*47*) and DISEMBL (*48*) are programs designed to identify disordered or unstructured regions of proteins. These programs were used for further analysis of the linker sequence to check for regions that are likely to be unstructured in solution. GLOBPLOT shows a curve with a flat to slightly positive slope for the linker region (not shown). Such a curve suggests a disordered, flexible structure. The slope of the C-terminal residues was larger than that of the N-terminal residues, suggesting that the N-terminal residues are less disordered than the C-terminal residues of the linker. GLOBPLOT indicated that residues 100−108 are a low-complexity sequence, in contrast to the results of PSIPRED.

DISEMBL (*46*) provides three different measures of protein disorder. All of the residues in the linker sequence fell into the "loops/coils" classification, which simply means that the sequence has a low likelihood of being either helical or a β-strand. This definition does not imply that the linker region lacks tertiary structure but rather that there is potential for it to lack structure. DISEMBL indicates that residues 54−88 and 105−128 are "hot loops", which are segments commonly found to have higher than average crystallographic *B*-factors in the Protein Data Bank. DISEMBL also marks residues 54−61, 81−111, and 120−128 disordered by the "remark465" definition, which are sequences of residues from structures deposited in the Protein Data Bank that commonly belong to regions that cannot be assigned to high-resolution portions of the electron density maps. Taken together, the analyses indeed suggest that some of the linker sequence of vitronectin lacks tertiary structure. The C-terminal region of the linker seems to be the region most likely to be structurally disordered in solution because it was identified by both DISEMBL and GLOBPLOT.

Structural Modeling. Analysis of the scattering data provided insight into the overall shape of vitronectin in solution. The consensus envelope produced by GA_STRUCT (*29*) is shown in two views in Figure 3. The overall length of the envelope is ~110 Å. The width is ~50 Å at the large end and ~40 Å at the small end of the structure. The narrowest point of the structure is ~35 Å. These widths are in rough agreement with the position of the peak in $P(r)$. The differences can be attributed to the structural averaging that occurs during generation of the consensus envelope by GA_STRUCT. The volume of the consensus envelope is ~111 000 Å^3. The volume estimated from the molecular weight of and partial specific volume[2] of vitronectin is 73 000 Å^3. The difference in volume can also be attributed to the structural averaging that produces the consensus envelope. Example model intensity profiles for individual models generated by GA_STRUCT are shown in Figure 2A with the data. The quality of the fit is good, having an average *F*

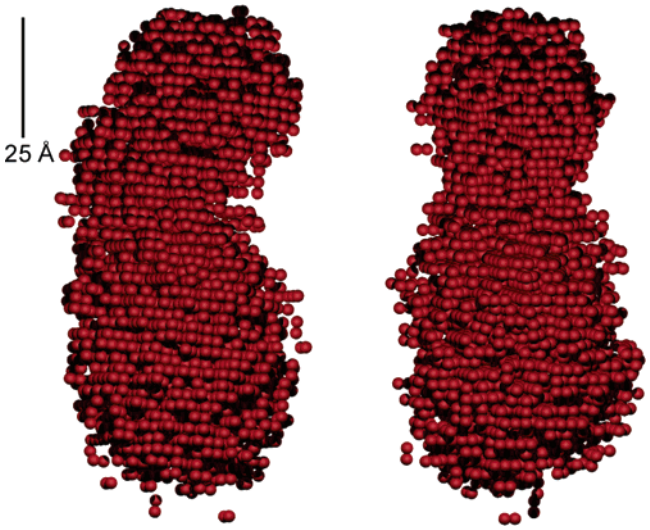

FIGURE 3: Consensus envelope model of vitronectin. The consensus envelope produced by GA_STRUCT (*29*) from the SAXS data is shown in two orthogonal views.

value of 0.634. Two additional runs of GA_STRUCT produced similar consensus envelope structures (not shown).

A different approach to analyzing the small-angle scattering data was pursued, in which structural models from threading (*14*) and the NMR structure of the SMB domain (*10*) were used, in combination with a cylinder to represent the volume of the unstructured linker region. The approximation of a flexible or unstructured region with a cylinder of appropriate volume has been successfully applied in developing models of protein kinase A from small-angle scattering data (*38*, *39*). The best-fit model produced by CONTRAST (*30*), having a cylinder with a radius of 12 Å, is shown in two views in Figure 4. The shape of the model is consistent with the consensus envelope, ignoring the contributions of the carbohydrates. The total molecular weight of the carbohydrates is low compared to that of the remainder of the structure, so it is not surprising that GA_STRUCT did not resolve any consistent structure for the carbohydrates. The other cylinder radii tested for the model produced similar results. The main difference lies in the angle of the SMB domain relative to the cylinder axis. In the case of the 10 Å cylinder (not shown), the long axis of this domain produces a more acute angle with the axis of the cylinder. As the cylinder radius increases to 20 Å, decreasing the length, the long axis of the SMB domain becomes nearly parallel to that of the cylinder. In all cases, the fit to the data is good, with F values ranging from 0.589 for the 12 Å radius cylinder to 0.614 for the 18 and 20 Å radius cylinders. The fact that the CONTRAST models fit the data as well as the GA_STRUCT model suggests that the structure adopts a relatively well-defined conformation in solution. To show the similarity of the structures, the high-resolution model is shown docked onto the consensus envelope in Figure 5. The general shapes of the structures agree well.

DISCUSSION

The organization of vitronectin into domains proposed originally on the basis of sequence alignment (*47*, *48*) was corroborated by our more recent application of threading, which predicted three domains in human plasma vitronectin (*14*). Docking of the central and C-terminal domains was constrained by an interdomain disulfide and provided instructive results regarding the heparin-binding site found on vitronectin at the juncture of these domains (*14*). However, the inability to model an intervening sequence of ~70 amino acids separating the N-terminal and central domains prohibited docking as an approach to modeling the full-length protein in this first computational work. In this study, we have predicted the relatively unstructured feature of this ~70-amino acid linker sequence using bioinformatic approaches. The mostly unstructured nature of this segment of the vitronectin sequence agrees with numerous studies showing this region to be highly susceptible to proteolysis (*14*).

An important step toward determining the solution structure for intact vitronectin has been achieved in this work using small-angle scattering measurements. The scattering data and subsequent modeling demonstrate that vitronectin is extended in solution, exhibiting a subtly bilobed shape. While the *ab initio* modeling by GA_STRUCT (*29*) provides no indication about the domain organization, the model built using the available information about the structures of vitronectin domains (from NMR and threading) with CONTRAST (*30*) is consistent with the scattering data and the *ab initio* model indicating the two-lobed structure. As one can see from Figure 5, the volume of the consensus envelope is somewhat larger than the volume occupied by the high-resolution model. In fact, the actual difference in volume is 37 000 Å^3. The apparently "empty" space, i.e., difference in volume, may be attributed to two different factors. First, the resulting consensus envelope is a structural average of several independent models. Second, a SAXS measurement observes the ensemble of structures present in the sample during the course of the exposure. As one can imagine, if the protein is flexible in solution, it will appear to occupy a larger volume.

Our calculations indicate an extended arrangement of domains, although it is possible that the N-terminal domain and linker sequence have an organization different from that suggested by the model. As an alternative, the SMB domain could be closer to the central domain, with the linker region wrapping around it and extending out the maximum distance determined from the scattering data. Such models were not tested, as it is clear that they cannot satisfy the scattering data in a manner that is in reasonable agreement with the model produced by GA_STRUCT. A much longer and thinner cylinder would be required to provide a length consistent with the d_{max} value of 110 Å determined from the $P(r)$ fitting if the density of the cylinder were kept the same as the remainder of the protein. Such a thin region would not allow the SMB domain to coil back toward the central and C-terminal domains in a physically realistic manner and remain consistent with the GA_STRUCT model. Another alternative is to allow the SMB domain to contact any point on the surface of the linker cylinder and to allow the cylinder to have any volume, with the requirement that the electron density be scaled appropriately to the volume. This approach, unfortunately, adds another degree of complexity to the modeling and would result in less robust models. The relatively simple approach taken here was chosen because it did not introduce more free parameters than necessary into the modeling.

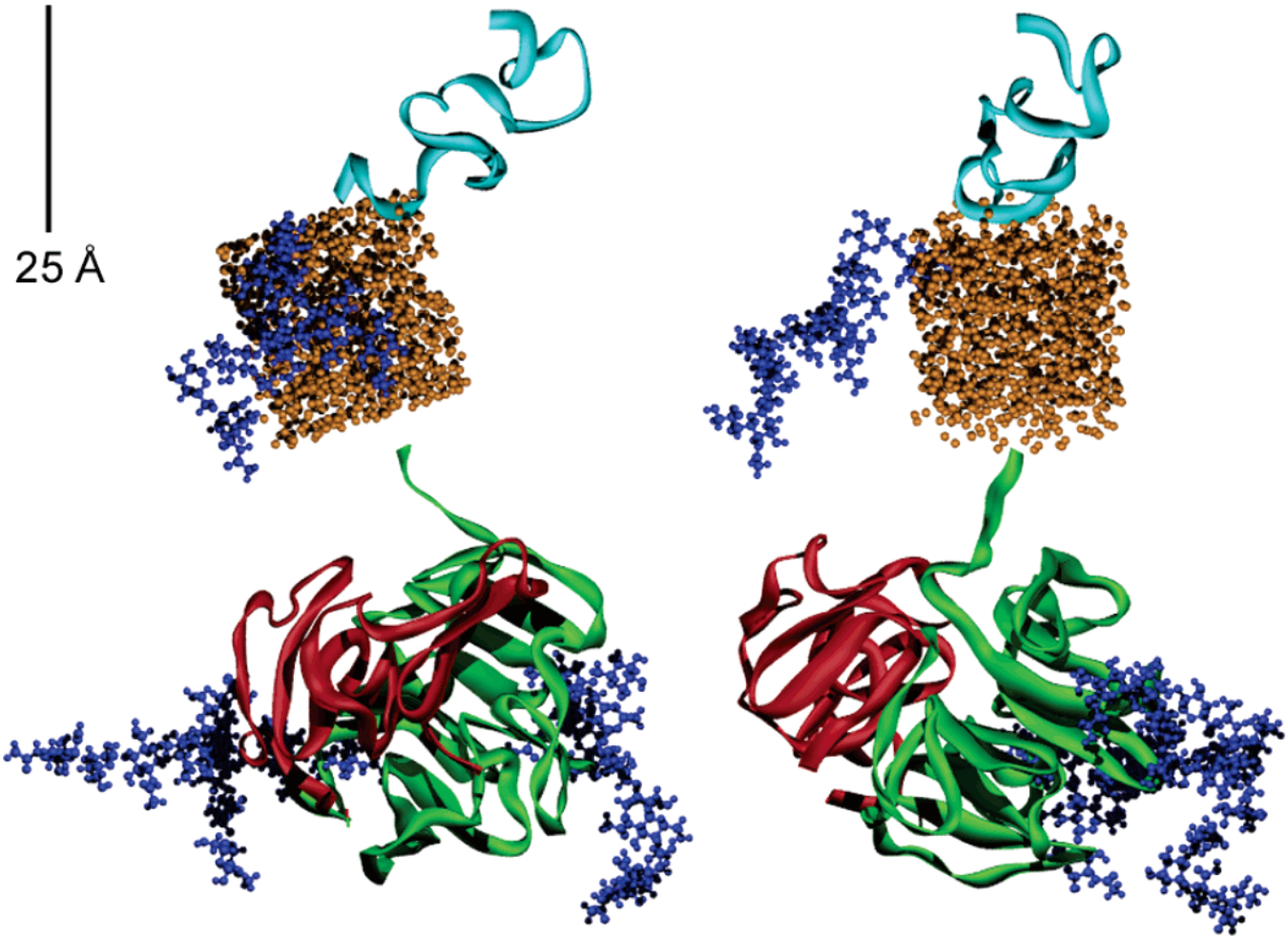

FIGURE 4: Vitronectin model using high-resolution structures. Shown in two orthogonal views is the model produced from the SAXS data by CONTRAST (*30*) using the available domain structures (Figure 1A) from NMR and threading, and the linker region as a cylinder with a radius of 12 Å. The somatomedin B domain is colored cyan, the linker region amber, the central domain green, the heparin-binding domain red, and the carbohydrates blue.

The model produced by CONTRAST (*30*) reveals some interesting features that are supported by other biochemical data. Importantly, the SMB domain is well-exposed to the surrounding solvent, making it accessible to various ligands. The high-affinity PAI-1-binding site in the SMB domain, which our NMR work has localized to the vicinity of the single α-helix in this cystine-rich domain (*10*), is highlighted in Figure 5 with the letter P. The binding site for the urokinase receptor overlaps extensively with this site comprising the α-helix (*10*, *13*). Our work using analytical ultracentrifugation (*49*) and monoclonal antibodies (*50*, *51*) indicates that PAI-1 binds in a 2:1 stoichiometry to vitronectin. Interestingly, other PAI-1-binding sites residing within the C-terminal domain have been proposed (*18*, *25*), and sigmoidal binding isotherms support the notion of allosteric PAI-1 binding effects (*52*). The structural model provides a clear separation between the high-affinity PAI-1-binding site in the SMB domain and a second lower-affinity site found elsewhere. The separation between the N- and C-terminal domains in the model shown in Figure 5 makes it conceivable for vitronectin to bind two PAI-1 molecules simultaneously without steric hindrance.

The binding site for an important class of cell-surface molecules, the integrin-type receptors, also is found within the N-terminal domain from residue 45 to 47. This site is denoted as the RGD tripeptide sequence in Figure 5. The juxtaposition of binding sites for PAI-1 and integrins has led to the idea that binding of the two is mutually exclusive. There is ample evidence that PAI-1 can compete with integrins for binding to vitronectin under some circumstances (*53*, *54*). We have recently characterized the assembly of higher-order PAI-1−vitronectin species and have shown that these multivalent complexes preferentially associate with the ECM and exhibit enhanced binding to purified integrins (*52*, *55*). These data demonstrate that vitronectin can bind simultaneously to PAI-1 and integrins under other circumstances.

Interestingly, our high-resolution structure for the SMB domain supports this possibility, with a PAI-1-binding surface that is separated from the RGD sequence (*10*). In the NMR structure, the RGD sequence from amino acid 45 to 47 lies within a flexible region of the structure (*10*). Nevertheless, it is unlikely to exhibit such a high degree of flexibility when covalently attached to the remainder of full-length vitronectin. In any case, it is interesting that the RGD sequence adjoins the relatively unstructured linker sequence between the N-terminal and central domains. In general, disordered regions of a protein may undergo disorder-to-order transitions upon binding to other molecules. Disordered regions may be involved in DNA recognition, modulation

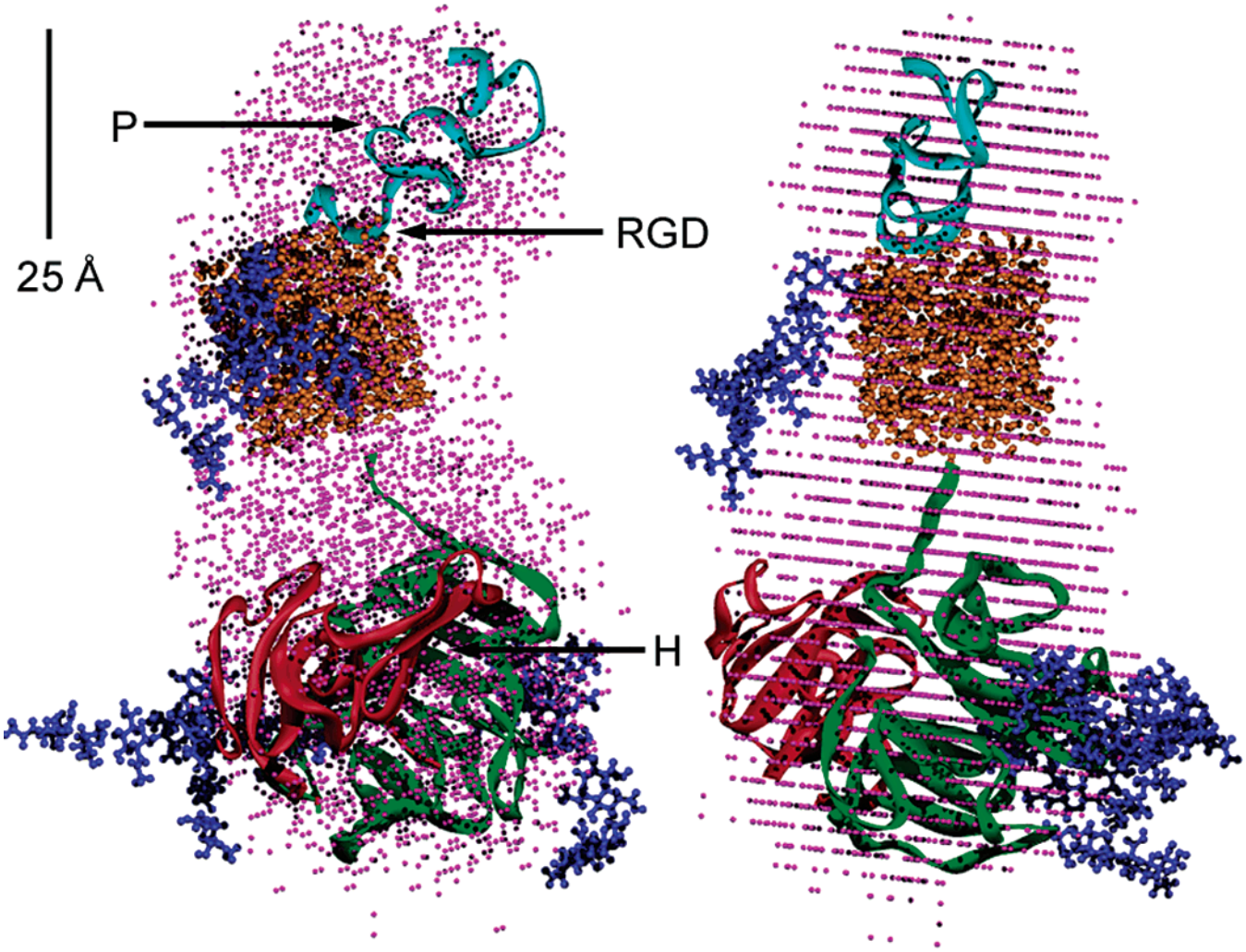

FIGURE 5: Comparison of the vitronectin models. Two orthogonal views of the model produced by CONTRAST (*30*) docked into the GA_STRUCT (*29*) consensus envelope. The somatomedin B domain is colored cyan, the linker region amber, the central domain green, the heparin-binding domain red, and the carbohydrates blue. The consensus envelope is colored violet. Binding sites for ligands are indicated with arrows and labels: P for PAI-1, RGD for integrins, and H for heparin.

of specificity and/or affinity of protein binding, molecular threading, activation by cleavage, or control of protein lifetimes (*56*). In the case of vitronectin, the disordered region is likely to play a role in modulation of the specificity and/or affinity of protein binding. For example, it may lend some conformational adaptability to the RGD sequence in vitronectin. This idea has some support from the work of Seiffert and co-workers, who suggest that heparin binding to a site near the C-terminus promotes a conformational change that more fully exposes the RGD sequence near the N-terminus (*57*).

The heparin-binding sequence, located at the interface between the central and C-terminal domains, is highlighted in Figure 5 with the letter H. The binding site for heparin is well-separated from the high-affinity PAI-1-binding site, as well as from receptor-binding sites for uPAR and integrins. The docked central and C-terminal domains are β-propeller structures (*14*), which have a well-established role in protein−protein interactions (*14*, *58*−*60*). We have hypothesized that the self-association of vitronectin, which occurs to produce the higher-ordered matrix-associated form of the molecule, is mediated through this region rich in β-sheets (*14*). In our model in which the binding of two PAI-1 molecules occurs en route to assembly of these higher-order complexes, the wide separation between the N- and C-terminal domains of vitronectin frees up significant room on the surface for additional contacts to form between the two vitronectin molecules in the complex. Multimeric forms of vitronectin have been shown to bind heparin more avidly (*19*, *61*); the structural model is provocative in this regard, since one can easily envision the lateral assembly of vitronectin multimers with adjacent heparin-binding sites that bind along the length of a heparin chain. We previously have proposed such a mechanism for multivalent, avid binding of heparin to vitronectin multimers (*19*), and the structural model supports this idea.

In conclusion, we have used small-angle scattering to elucidate the shape of the human plasma vitronectin monomer. These results are the first to produce a model for the three-dimensional structure of human plasma vitronectin in solution under near-physiological conditions. The protein adopts an extended conformation, and the models provide useful information about the domain organization of the protein that is consistent with other data regarding binding partners for vitronectin. The structure of the vitronectin monomer will serve as a foundation for further studies on complexes of vitronectin and its various binding partners. In the modern world of structural biology, the characteriza-

tion of biologically relevant complexes is needed, and similar small-angle scattering approaches are well suited to characterizing these higher-order complexes with more than one constituent.

ACKNOWLEDGMENT

G.W.L. thanks J. S. Lin for his assistance and many useful discussions at Oak Ridge National Laboratory. We also thank Lin Yang for technical assistance with small-angle X-ray scattering measurements at the National Synchrotron Light Source and Nikki Ball for assistance with protein preparation for these experiments. We are also indebted to Dr. George Wignall (Oak Ridge National Laboratory) for support and encouragement during the course of this work. Also, we appreciate our former colleague, Dr. Dong Xu, presently at the University of Missouri (Columbia, MO), for the initial work on disorder predictions and for helpful comments about the manuscript. Research was carried out in part at the X21 beamline of the National Synchrotron Light Source, which is supported by the U.S. Department of Energy, Division of Materials Sciences and Division of Chemical Sciences, under Contract DE-AC02-98CH10886.

REFERENCES

1. Preissner, K. T. (1991) Structure and biological role of vitronectin, *Annu. Rev. Cell Biol. 7*, 275−310.
2. Preissner, K. T., and Seiffert, D. (1998) Role of vitronectin and its receptors in haemostasis and vascular remodeling, *Thromb. Res. 89*, 1−21.
3. Andreasen, P. A., Kjoller, L., Christensen, L., and Duffy, M. J. (1997) The urokinase-type plasminogen activator system in cancer metastasis: A review, *Int. J. Cancer 72*, 1−22.
4. Waltz, D. A., Natkin, L. R., Fujita, R. M., Wei, Y., and Chapman, H. A. (1997) Plasmin and plasminogen activator inhibitor type 1 promote cellular motility by regulating the interaction between the urokinase receptor and vitronectin, *J. Clin. Invest. 100*, 58−67.
5. Declerck, P. J., De Mol, M., Alessi, M. C., Baudner, S., Paques, E. P., Preissner, K. T., Muller-Berghaus, G., and Collen, D. (1988) Purification and characterization of a plasminogen activator inhibitor 1 binding protein from human plasma. Identification as a multimeric form of S protein (vitronectin), *J. Biol. Chem. 263*, 15454−15461.
6. Schvartz, I., Seger, D., and Shaltiel, S. (1999) Vitronectin, *Int. J. Biochem. Cell Biol. 31*, 539−544.
7. Horn, N. A., Hurst, G. B., Mayasundari, A., Whittemore, N. A., Serpersu, E. H., and Peterson, C. B. (2004) Assignment of the four disulfides in the N-terminal somatomedin B domain of native vitronectin isolated from human plasma, *J. Biol. Chem. 279*, 35867−35878.
8. Deng, G., Royle, G., Wang, S., Crain, K., and Loskutoff, D. J. (1996) Structural and functional analysis of the plasminogen activator inhibitor-1 binding motif in the somatomedin B domain of vitronectin, *J. Biol. Chem. 271*, 12716−12723.
9. Seiffert, D., and Loskutoff, D. J. (1991) Evidence that type 1 plasminogen activator inhibitor binds to the somatomedin B domain of vitronectin, *J. Biol. Chem. 266*, 2824−2830.
10. Mayasundari, A., Whittemore, N. A., Serpersu, E. H., and Peterson, C. B. (2004) The solution structure of the N-terminal domain of human vitronectin: Proximal sites that regulate fibrinolysis and cell migration, *J. Biol. Chem. 279*, 29359−29366.
11. Gibson, A., Baburaj, K., Day, D. E., Verhamme, I., Shore, J. D., and Peterson, C. B. (1997) The use of fluorescent probes to characterize conformational changes in the interaction between vitronectin and plasminogen activator inhibitor-1, *J. Biol. Chem. 272*, 5112−5121.
12. Cherny, R. C., Honan, M. A., and Thiagarajan, P. (1993) Site-directed mutagenesis of the arginine-glycine-aspartic acid in vitronectin abolishes cell adhesion, *J. Biol. Chem. 268*, 9725−9729.
13. Deng, G., Curriden, S. A., Wang, S., Rosenberg, S., and Loskutoff, D. J. (1996) Is plasminogen activator inhibitor-1 the molecular switch that governs urokinase receptor-mediated cell adhesion and release? *J. Cell Biol. 134*, 1563−1571.
14. Xu, D., Baburaj, K., Peterson, C. B., and Xu, Y. (2001) Model for the three-dimensional structure of vitronectin: Predictions for the multi-domain protein from threading and docking, *Proteins 44*, 312−320.
15. Liang, O. D., Maccarana, M., Flock, J. I., Paulsson, M., Preissner, K. T., and Wadstrom, T. (1993) Multiple interactions between human vitronectin and *Staphylococcus aureus*, *Biochim. Biophys. Acta 1225*, 57−63.
16. Liang, O. D., Preissner, K. T., and Chhatwal, G. S. (1997) The hemopexin-type repeats of human vitronectin are recognized by *Streptococcus pyogenes*, *Biochem. Biophys. Res. Commun. 234*, 445−449.
17. Liang, O. D., Rosenblatt, S., Chhatwal, G. S., and Preissner, K. T. (1997) Identification of novel heparin-binding domains of vitronectin, *FEBS Lett. 407*, 169−172.
18. Kost, C., Stuber, W., Ehrlich, H. J., Pannekoek, H., and Preissner, K. T. (1992) Mapping of binding sites for heparin, plasminogen activator inhibitor-1, and plasminogen to vitronectin's heparin-binding region reveals a novel vitronectin-dependent feedback mechanism for the control of plasmin formation, *J. Biol. Chem. 267*, 12098−12105.
19. Zhuang, P., Chen, A. I., and Peterson, C. B. (1997) Native and multimeric vitronectin exhibit similar affinity for heparin. Differences in heparin binding properties induced upon denaturation are due to self-association into a multivalent form, *J. Biol. Chem. 272*, 6858−6867.
20. Preissner, K. T. (1990) Specific binding of plasminogen to vitronectin. Evidence for a modulatory role of vitronectin on fibrin-(ogen)-induced plasmin formation by tissue plasminogen activator, *Biochem. Biophys. Res. Commun. 168*, 966−971.
21. Tschopp, J., Masson, D., Schafer, S., Peitsch, M., and Preissner, K. T. (1988) The heparin binding domain of S-protein/vitronectin binds to complement components C7, C8, and C9 and perforin from cytolytic T-cells and inhibits their lytic activities, *Biochemistry 27*, 4103−4109.
22. Milis, L., Morris, C. A., Sheehan, M. C., Charlesworth, J. A., and Pussell, B. A. (1993) Vitronectin-mediated inhibition of complement: Evidence for different binding sites for C5b-7 and C9, *Clin. Exp. Immunol. 92*, 114−119.
23. Preissner, K. T., Grulich-Henn, J., Ehrlich, H. J., Declerck, P., Justus, C., Collen, D., Pannekoek, H., and Muller-Berghaus, G. (1990) Structural requirements for the extracellular interaction of plasminogen activator inhibitor 1 with endothelial cell matrix-associated vitronectin, *J. Biol. Chem. 265*, 18490−18498.
24. Chain, D., Korc-Grodzicki, B., Kreizman, T., and Shaltiel, S. (1991) Endogenous cleavage of the Arg-379-Ala-380 bond in vitronectin results in a distinct conformational change which 'buries' Ser-378, its site of phosphorylation by protein kinase A, *Biochem. J. 274*, 387−394.
25. Gechtman, Z., Sharma, R., Kreizman, T., Fridkin, M., and Shaltiel, S. (1993) Synthetic peptides derived from the sequence around the plasmin cleavage site in vitronectin. Use in mapping the PAI-1 binding site, *FEBS Lett. 315*, 293−297.
26. Zhou, A., Huntington, J. A., Pannu, N. S., Carrell, R. W., and Read, R. J. (2003) How vitronectin binds PAI-1 to modulate fibrinolysis and cell migration, *Nat. Struct. Biol. 10*, 541−544.
27. Kamikubo, Y., Okumura, Y., and Loskutoff, D. J. (2002) Identification of the disulfide bonds in the recombinant somatomedin B domain of human vitronectin, *J. Biol. Chem. 277*, 27109−27119.
28. Kamikubo, Y., De Guzman, R., Kroon, G., Curriden, S., Neels, J. G., Churchill, M. J., Dawson, P., Oldqiej, S., Jagielska, A., Sheraga, H. A., Loskutoff, D. J., and Dyson, H. J. (2004) Disulfide bonding aarrangements in active forms of the somatomedin B domain of human vitronectin, *Biochemistry 43*, 6519−6534.
29. Heller, W. T., Krueger, J. K., and Trewhella, J. (2003) Further insights into calmodulin-myosin light chain kinase interaction from solution scattering and shape restoration, *Biochemistry 42*, 10579−10588.
30. Heller, W. T., Abusamhadneh, E., Finley, N., Rosevear, P. R., and Trewhella, J. (2002) The solution structure of a cardiac troponin C-troponin I-troponin T complex shows a somewhat compact troponin C interacting with an extended troponin I-troponin T component, *Biochemistry 41*, 15654−15663.

31. Dahlback, B., and Podack, E. R. (1985) Characterization of human S protein, an inhibitor of the membrane attack complex of complement. Demonstration of a free reactive thiol group, *Biochemistry 24*, 2368−2374.
32. Zhuang, P., Blackburn, M. N., and Peterson, C. B. (1996) Characterization of the denaturation and renaturation of human plasma vitronectin. I. Biophysical characterization of protein unfolding and multimerization, *J. Biol. Chem. 271*, 14323−14332.
33. Hendricks, R. W. (1978) The Oak Ridge National Laboratory 10-meter small-angle X-ray scattering camera, *J. Appl. Crystallogr. 11*, 15−30.
34. Russell, T. P., Lin, J. S., Spooner, S., and Wignall, G. D. (1988) Intercalibration of small-angle X-ray and neutron scattering data, *J. Appl. Crystallogr. 21*, 629−638.
35. Guinier, A., and Fournet, G. (1955) *Small-Angle Scattering of X-rays*, John Wiley & Sons, New York.
36. Debye, P., and Beuche, A. M. (1949) Scattering by an inhomogeneous solid, *J. Appl. Phys. 20*, 518−525.
37. Moore, P. B. (1980) Small-angle scattering. Information content and error analysis, *J. Appl. Crystallogr. 13*, 168−175.
38. Heller, W. T., Vigil, D., Brown, S., Blumenthal, D. K., Taylor, S. S., and Trewhella, J. (2004) C Subunits Binding to the Protein Kinase A RIα Dimer Induces a Large Conformational Change, *J. Biol. Chem. 279*, 19084−19090.
39. Vigil, D., Blumenthal, D. K., Heller, W. T., Brown, S., Taylor, S. S., and Trewhella, J. (2004) Solution Structures and Conformational Changes of the Type Iα, IIα and IIβ Protein Kinase A Regulatory Subunit Homodimers: Role of the Linker Regions, *J. Mol. Biol. 337*, 1183−1194.
40. Bohne, A., Lang, E., and von der Leith, C.-W. (1998) Carbohydrate Modeling by Internet, *J. Mol. Model. 4*, 33−43.
41. Li, X., Romero, P., Rani, M., Dunker, A. K., and Obradovic, Z. (1999) Predicting protein disorder for N-, C-, and internal regions, *Genome Inf. 10*, 30−40.
42. Romero, P., Obradovic, Z., Li, X., Garner, E., Brown, C., and Dunker, A. K. (2001) Sequence complexity of disordered protein, *Proteins: Struct., Funct., Genet. 42*, 38−48.
43. McGuffin, L. J., Bryson, K., and Jones, D. T. (2000) The PSIPRED Protein Structure Prediction Server, *Bioinformatics 16*, 404−405.
44. Jones, D. T. (1999) Protein secondary structure prediction based on position specific scoring matrices, *J. Mol. Biol. 292*, 195−202.
45. Linding, R., Russell, R. B., Neduva, V., and Gibson, T. J. (2003) GlobPlot: Exploring protein sequences for globularity and disorder, *Nucleic Acids Res. 31*, 3701−3708.
46. Linding, R., Jensen, L. J., Diella, F., Bork, P., Gibson, T. J., and Russell, R. B. (2003) Protein disorder prediction: Implications for structural proteomics, *Structure 11*, 1453−1459.
47. Suzuki, S., Pierschbacher, M. D., Hayman, E. G., Nguyen, K., Ohgren, Y., and Ruoslahti, E. (1984) Domain structure of vitronectin. Alignment of active sites, *J. Biol. Chem. 259*, 15307−15314.
48. Hunt, L. T., Barker, W. C., and Chen, H. R. (1987) A domain structure common to hemopexin, vitronectin, interstitial collagenase, and a collagenase homolog, *Protein Sequences Data Anal. 1*, 21−26.
49. Podor, T. J., Shaughnessy, S. G., Blackburn, M. N., and Peterson, C. B. (2000) New insights into the size and stoichiometry of the plasminogen activator inhibitor type-1·vitronectin complex, *J. Biol. Chem. 275*, 25402−25410.
50. Podor, T. J., Campbell, S., Chindemi, P., Foulon, D. M., Farrell, D. H., Walton, P. D., Weitz, J. I., and Peterson, C. B. (2002) Incorporation of vitronectin into fibrin clots: Evidence for a binding interaction between vitronectin and γA/γ' fibrinogen, *J. Biol. Chem. 277*, 7520−7528.
51. Podor, T. J., Peterson, C. B., Lawrence, D. A., Stefansson, S., Shaughnessy, S. G., Foulon, D. M., Butcher, M., and Weitz, J. I. (2000) Type 1 plasminogen activator inhibitor binds to fibrin via vitronectin, *J. Biol. Chem. 275*, 19788−19794.
52. Minor, K. H., and Peterson, C. B. (2002) PAI-1 promotes the self-association of vitronectin into complexes exhibiting altered incorporation into the extracellular matrix, *J. Biol. Chem. 277*, 10337−10345.
53. Stefansson, S., and Lawrence, D. A. (1996) The serpin PAI-1 inhibits cell migration by blocking integrin αVβ3 binding to vitronectin, *Nature 383*, 441−443.
54. Loskutoff, D. J., Curriden, S. A., Hu, G., and Deng, G. (1999) Regulation of cell adhesion by PAI-1, *Apmis 107*, 54−61.
55. Minor, K. H., Wilkins-Port, C. E., McKeown-Longo, P. J., and Peterson, C. B. (2004) Plasminogen activator inhibitor-1 alters the binding and degradation of vitronectin by cultured human fibroblasts, *Biochim. Biophys. Acta* (submitted for publication).
56. Dunker, A. K., Garner, E., Guilliot, S., Romero, P., Albrecht, K., Hart, J., Obradovic, Z., Kissinger, C., and Villafranca, J. E. (1998) Protein disorder and the evolution of molecular recognition: Theory, predictions and observations, *Pac. Symp. Biocomput.*, 473−484.
57. Seiffert, D., and Smith, J. W. (1997) The cell adhesion domain in plasma vitronectin is cryptic, *J. Biol. Chem. 272*, 13705−13710.
58. Beisel, H. G., Kawabata, S., Iwanaga, S., Huber, R., and Bode, W. (1999) Tachylectin 2: Crystal structure of a specific GlcNAc/GalNAc-binding lectin involved in the innate immunity host defense of the Japanese horseshoe crab *Tachypleus tridentatus*, *EMBO J. 18*, 2313−2322.
59. Wall, M. A., Posner, B. A., and Sprang, S. R. (1998) Structural basis of activity and subunit recognition in G protein heterotrimers, *Structure 6*, 1169−1183.
60. Xiong, J. P., Stehle, T., Diefenbach, B., Zhang, R., Dunker, R., Scott, D. L., Joachimiak, A., Goodman, S. L., and Arnaout, M. A. (2001) Crystal structure of the extracellular segment of integrin αVβ3, *Science 294*, 339−345.
61. Peterson, C. B. (1998) Binding sites on native and multimeric vitronectin exhibit similar affinity for heparin. The influence of self-association and multivalence on ligand binding, *Trends Cardiovasc. Med. 8*, 124−131.
62. Harpaz, Y., Gerstein, M., and Chothia, C. (1994) Volume changes on protein folding, *Structure 2*, 641−649.

BI048347S